Enzyme-inspired Ligand Engineering of Gold Nanoclusters for Electrocatalytic Microenvironment Manipulation

Zhihe Liu[†,§], Junmei Chen[†], Bo Li[⊥], De-en Jiang[⊥,*], Lei Wang[†,*], Qiaofeng Yao[‡,¶,*], and Jianping Xie[†,§,*]

† Department of Chemical and Biomolecular Engineering, National University of Singapore, 117585, Singapore

‡ Key Laboratory of Organic Integrated Circuits, Ministry of Education & Tianjin Key Laboratory of Molecular Optoelectronic Sciences, Department of Chemistry, School of Science, Tianjin University, Tianjin 300072, China

¶ Collaborative Innovation Center of Chemical Science and Engineering (Tianjin), Tianjin 300072, China

§ Joint School of National University of Singapore and Tianjin University International Campus of Tianjin University Binhai New City, Fuzhou 350207, P. R. China

⊥ Department of Chemical and Biomolecular Engineering, Vanderbilt University, Nashville, TN, 37212, USA

Keywords: (enzyme, ligand engineering, metal nanoclusters, electrocatalysts, microenvironment)

Abstract

Natural enzymes intricately regulate substrate accessibility through specific amino acid sequences and folded structures at their active sites. Achieving such precise control over the microenvironment has proven to be challenging in nanocatalysis, especially in the realm of ligand-stabilized metal nanoparticles. Here, we use atomically precise metal nanoclusters (NCs) as model catalysts to demonstrate an effective ligand engineering strategy to control the local concentration of CO_2 on the surface of gold (Au) NCs during electrocatalytic CO_2 reduction reactions (CO_2RR). The precise incorporation of two 2-thiouracil-5-carboxylic acid (TCA) ligands within the pocket-like cavity of $[Au_{25}(p\text{MBA})_{18}]^-$ NCs (*p*MBA = *para*-mercaptobenzoic acid) leads to a substantial acceleration in the reaction kinetics of CO_2RR. This enhancement is attributed to a more favourable microenvironment in proximity to the active site for CO_2, facilitated by supramolecular interactions between the nucleophilic $N^{\delta-}$ of the pyrimidine ring of the TCA ligand and the electrophilic $C^{\delta+}$ of CO_2. A comprehensive investigation employing absorption spectroscopy, mass spectrometry, isotopic labelling measurements, electrochemical analyses, and quantum chemical computation highlights the pivotal role of local CO_2 enrichment in enhancing the activity and selectivity of TCA-modified Au_{25} NCs for CO_2RR. Notably, a high Faradaic efficiency of 98.6% toward CO has been achieved. The surface engineering approach and catalytic fundamentals elucidated in this study provide a systematic foundation for the molecular-level design of metal-based electrocatalysts.

Introduction

Enzymes typically utilize specific functional groups, such as amino groups, to tailor the microenvironment around their active metal sites.[1, 2] The spatial arrangement of these moieties significantly influences how substrate molecules approach the active sites during the initial stages of catalytic reactions. Such precise manipulation of the microenvironment is a crucial aspect of enzymatic chemistry, and there is a strong desire for a comparable level of control in inorganic catalysis, which allows for the rational customization of catalytic activity and selectivity in inorganic catalysts. However, microenvironment engineering has rarely been investigated at the molecular level, as previous reports have predominantly focused on engineering the active sites of metal-based catalysts to promote activity and selectivity.[3] Atomically precise metal nanoclusters (NCs) represent an emerging class of ultra-small particles with a typical core size of 2 nm or less.[4-9] Recent advancements in X-ray crystallography reveal that metal NCs exhibit similar structural complexity and hierarchy as those of natural proteins, positioning them as ideal model catalysts to mimic the intricate catalytic performance of enzymes.[10] In addition to the protein-like structural hierarchy, strong quantum confinement effects in this ultra-small size regime also render metal NCs with several intriguing molecule-like properties, such as discrete energy levels, quantized charging, and redox behaviors.[11] These physicochemical properties, governed by the size and structure of metal NCs at the atomic level, provide a valuable avenue for studying catalytic reactions occurring on the surface of metal NCs.

Due to their protein-like structure, metal NCs have been widely employed as enzyme mimics for catalysing conversion reactions of crucial molecules in sustainability research, with CO_2 as a good example. Taking the most investigated $[Au_{25}(SR)_{18}]^-$ NC (SR = thiolate ligand) as an example, it consists of an icosahedral Au_{13} core, whose 12 out of 20 triangular facets are capped by six staple-like SR–[Au(I)–SR]$_2$ motifs.[12, 13] Combined X-ray crystallography and computational simulations indicate that the arrangement of three core Au atoms, three motif Au atoms, and three SR ligands can create pocket-like cavities on the surface of $[Au_{25}(SR)_{18}]^-$ NCs. These cavities function as nanoreactors for the electrocatalytic reduction of CO_2 (CO_2RR). The protecting ligands of Au NCs (i.e., SR ligands) are crucial constituents of the pocket-like cavities in Au NCs, which can be tailored to enhance the activity and selectivity in CO_2RR.[14-17] For example, Zang group observed that thiolate-protected

Au_{28} NCs demonstrated better CO_2RR activity than Au_{28} NCs capped with alkynyl ligands.[18] In another study, Jin group explored the effect of ligand anchoring point on the selectivity of Au NCs for CO.[19] The majority of documented studies have focused on the effects of SR ligands on the electronic structure of catalytically active Au sites, with limited exploration of how ligands influence the accessibility of CO_2 molecules. Given that numerous enzymatic reactions are known to be diffusion-control,[20-22] it becomes crucial to unravel the effects of ligands on the mass transfer of CO_2 at the molecular level.

Due to the limited solubility of CO_2 in aqueous electrolyte (~34 mM), CO_2RR is susceptible to a CO_2 diffusion-controlled process. Recent studies also found that the local concentration surrounding the catalytically active sites was considerably low,[23-26] leading to unsatisfactory reaction kinetics.[27, 28] To tackle this challenging issue, several strategies have been developed to engineer the microenvironment of CO_2RR on the surface of metal-based nanocatalysts.[3, 29, 30] As an example, the customization of cations in the electrolyte at the outer Helmholtz layer allows for the effective tuning of the double electrical layer and local pH surrounding the nanocatalysts, providing a promising method for controlling the reaction rate or selectivity in electrocatalytic processes.[31, 32] Moreover, enhancing the hydrophobic properties of the electrocatalyst surface facilitates the reduction of the thickness of the CO_2 diffusion layer and lowers the activation energy barrier for CO_2.[33] More recently, Sargent group has also developed a nanostructured gold tip electrode that, under catalytic conditions, generates high electric fields.[34] In this manner, electrolyte cations can accumulate around the active sites, enriching the local CO_2 concentration and accelerating the reaction kinetics of CO_2RR. However, challenges remain in improving local CO_2 concentration through the modulation of organic molecules, hindering the atom-by-atom customization of metal-based electrocatalysts for CO_2RR.

Herein, we developed an atomically precise surface engineering strategy for enhancing the local concentration of CO_2 near the active sites of metal NCs, which led to a substantial acceleration of the electrocatalytic kinetics of metal-based electrocatalysts for aqueous CO_2RR. Recently, nitrogen-doped polymers have been widely employed for CO_2 capture, owing to the strengthened interactions between electronegative N (i.e., $N^{\delta-}$) and electropositive C (i.e., $C^{\delta+}$) of CO_2.[35-38] We therefore hypothesized that the incorporation of thiolate ligands containing a nitrogen-

heterocyclic ring into the pocket-like cavity of metal NCs might be able to increase local CO_2 concentration, consequently enhancing the CO_2RR performance. By using atomically precise $[Au_{25}(p\text{MBA})_{18}]^-$ NCs (*p*MBA = *para*-mercaptobenzoic acid) as model clusters, we selectively replaced two *p*MBA ligands with pyrimidine-containing thiolate ligands, namely 2-thiouracil-5-carboxylic acid (abbreviated as TCA). A combination of experimental and computational investigations suggests that the incorporation of two TCA ligands accelerates the mass transfer of CO_2 from the protecting ligand shell to the active Au centers, significantly increasing the local CO_2 concentration near the pocket-like cavity of $[Au_{25}(SR)_{18}]^-$ NCs. The enhanced local CO_2 concentration readily transmits into an improved electrocatalytic performance of $[Au_{25}(SR)_{18}]^-$ in CO_2RR, delivering a close-to-unit Faradaic efficiency (FE) of CO_2 to CO (98.6% at –0.9 V), a low overpotential (660 mV for a CO partial current density of 10 mA/cm^2), and an appreciable turnover frequency (39 s^{-1}). This work exemplifies the efficacy of enzyme-like microenvironment engineering through delicate ligand control to regulate the mass transfer profile of substrate molecules. The findings suggest that, besides active site engineering, controlling microenvironment around the active sites could provide an alternative avenue for promoting the electrocatalytic performance of metal nanoparticles or NCs.

Results and Discussion

$[Au_{25}(p\text{MBA})_{18}]^-$ NCs were synthesized using a CO-reduction method following our reported protocol with minor modifications.[39] The incorporation of TCA onto Au_{25} NCs was achieved through an *in-situ* growth method, where aliquots of *p*MBA ligands were replaced by TCA in the CO-reduction method (refer to the section Methods for more details). The resulting $[Au_{25}(p\text{MBA})_{18}]^-$ NCs are reddish-brown in aqueous solution and exhibit characteristic absorption features of pure $[Au_{25}(SR)_{18}]^-$ NCs. The absorption peaks are located at 430, 460, 575, 690, and 815 nm in the ultraviolet-visible (UV-vis) absorption spectrum in Figure 1a, consistent with our reported results.[39] After the introduction of TCA, the raw aqueous solution also retains a similar reddish-brown color. Distinct absorption peaks were also observed at the same positions as those of $[Au_{25}(p\text{MBA})_{18}]^-$ NCs, confirming the successful synthesis of $[Au_{25}(SR)_{18}]^-$ NCs. The successful incorporation of TCA into the protecting shell of $[Au_{25}(p\text{MBA})_{18-x}(\text{TCA})_x]^-$

NCs was further verified by Fourier transform infrared (FT-IR) spectroscopy (Figure 1b), where a notable band corresponding to N-H bending in the pyrimidine ring was distinctly observed at 1531 cm^{-1}. Electrospray ionization mass spectrometry (ESI-MS, in negative ion mode) was used to further confirm the precise molecular formula of the obtained Au NCs. The ESI-MS spectrum of $[Au_{25}(pMBA)_{18}]^-$ NCs shows three sets of peaks within the m/z range of 1000-4000, which account for Au_{25} NCs capped by *p*MBA carrying 7, 6, and 5 negative charges, respectively (Figure 1c). The isotope distribution of the base peak (green line) matches well with the simulated isotope distribution of $[Au_{25}(pMBA)_{18}–6H]^{7-}$ (filled peaks) (Figure 1c, inset). Regarding the ESI-MS spectra of Au_{25} NCs co-protected by *p*MBA and TCA, three sets of peaks corresponding to Au_{25} NCs with 7, 6, 5 negative charges were also observed in their ESI-MS spectra (Figure 1d). A zoom-in spectrum reveals some additional peaks compared to $[Au_{25}(pMBA)_{18}]^-$ (Figure S1), originating from the replacement of one or two *p*MBA ligands by TCA ligands, i.e., $[Au_{25}(pMBA)_{18-x}(TCA)_x]^-$ (x = 1 or 2). A distinguished isotope distribution of the base peak (blue line) located at ~1285.2 (Figure 1d, inset) matches well with the simulated isotope distribution of $[Au_{25}(pMBA)_{16}(TCA)_2–5H]^{6-}$ (filled peaks), confirming the successful formation of $[Au_{25}(pMBA)_{16}(TCA)_2]^-$. Further increasing the parent molar proportion of TCA led to an increase in the substituted numbers without changing the formula, $[Au_{25}(SR)_{18}]^-$ as suggested by UV-vis absorption spectrum and ESI-MS spectra (Figure S2).

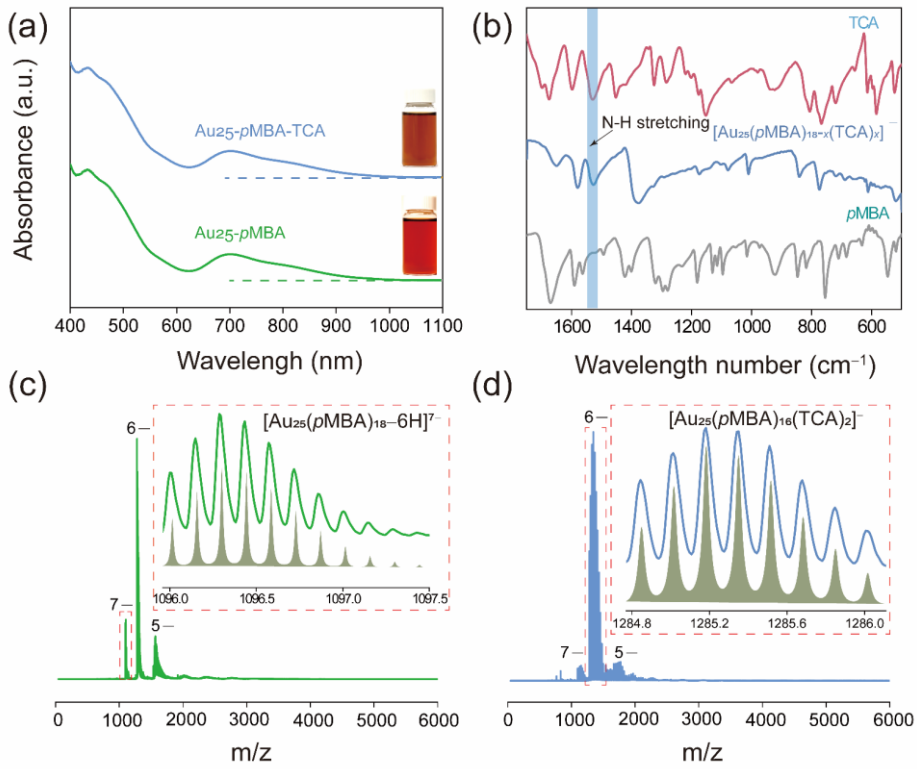

Figure 1. Characterizations of Au_{25} NCs capped by *p*MBA and *p*MBA/TCA. (a) Ultraviolet–visible absorption spectra (inset digital photo is the raw Au_{25} aqueous solution). (b) Fourier transform infrared (FT-IR) spectra of *p*MBA, TCA, and Au_{25} NCs capped by *p*MBA/TCA. (c) and (d) Electrospray ionization mass spectra of Au_{25} NCs capped by *p*MBA and *p*MBA/TCA. The inset shows the zoom-in mass spectrum marked by a red dashed rectangle (the filled peaks in inset belong to the simulated isotope distribution peaks).

To gain molecular insights into ligand distribution on the Au_{25} NC surface, nuclear magnetic resonance (NMR) spectroscopy was employed to probe the surface environment of Au_{25} NCs (Figure 2). Both ^{1}H NMR and 2D ^{1}H-^{1}H nuclear Overhauser effect spectroscopy (NOESY) were conducted to deduce the surface ligand distribution by analysing the detailed spatial coupling of these two ligands. In the ^{1}H NMR spectra, the signals from *p*MBA of $[Au_{25}(pMBA)_{18}]^-$ NCs were split into two sets of peaks, indicating two different chemical environments of *p*MBA ligands on the cluster surface. This is in good accordance to the two types of SR ligands in the SR-[Au(I)-SR]$_2$ motifs, where the vertex-type SR coordinates to two motif Au atoms, while the edge-type SR

coordinates to both motif and core Au atoms (Figure 2a).[40] As shown in Figure 2b, the peaks at δ = 7.53 and 7.38 ppm are attributed to H_A' and H_B' of edge-type *p*MBA ligands (superscript ' indicates edge-type SR), respectively, while the peaks at δ = 7.45 and 7.25 ppm should be attributed to H_A and H_B of vertex-type *p*MBA ligands. Such assignment was further verified by peak area analysis, where the integral area ratio of H_A and H_A' peaks is 0.51, closely resembling the theoretical ratio of 0.5. In sharp contrast, an addition peak at δ = 7.50 ppm was observed in the ^{1}H NMR spectrum of $[Au_{25}(pMBA)_{18-x}(TCA)_x]^-$, which stems from the H_C resonance of TCA ligands. For easy reference, the ^{1}H NMR spectra of free *p*MBA and TCA are depicted in Figure 2b. Furthermore, the area ratio of H_A/H_A' from *p*MBA ligands is below 2/1, clearly indicating the partial replacement of edge-type *p*MBA by TCA. More importantly, a clear cross-peak between H_C of TCA and H_B' of *p*MBA was observed in the 2D ^{1}H-^{1}H NOESY spectrum of $[Au_{25}(pMBA)_{18-x}(TCA)_x]^-$ NCs, (Figure 2b and 2c), probably due to the spatial proximity of TCA ligand to the edge-type *p*MBA ligand from the neighbouring SR-[Au(I)-SR]$_2$ motif. This observation aligns well with the incorporation of TCAs on the edge sites of SR-[Au(I)-SR]$_2$ motifs. The major factor that determines the favorable positioning of TCA is how comparable steric hindrance is to *p*MBA. This phenomenon can be explained by a proposed ligand exchange mechanism.[41] The average distance between close inter-staple Au-S_{edge} (3.92 Å) and S_{edge}-S_{edge} (5.01 Å) is shorter than that of Au-S_{vertex} (6.23 Å) and S_{vertex}-S_{vertex} (8.50 Å), respectively. This suggests that there is less steric hindrance around the edge sulphur than the vertex sulphur. In this scenario, ligands with greater steric hindrance might preferentially arrange themselves at the vertex rather than the edge. In addition, we conducted X-ray photo-electron spectroscopy (XPS) measurements to investigate the Au valence states of Au_{25} NCs before and after the incorporation of TCA ligands. As shown in Figure S3, the high-resolution XPS spectra of Au 4f reveal a negative shift of ~0.197 eV after the incorporation of TCA ligands, indicating a profound electron flow from TCA to $[Au_{25}(pMBA)_{18-x}(TCA)_x]^-$. A typical peak of pyrimidine nitrogen located at ~400.3 eV was also observed in the XPS spectrum of $[Au_{25}(pMBA)_{18-x}(TCA)_x]^-$ (Figure S4), supporting the presence of TCA on the cluster surface.

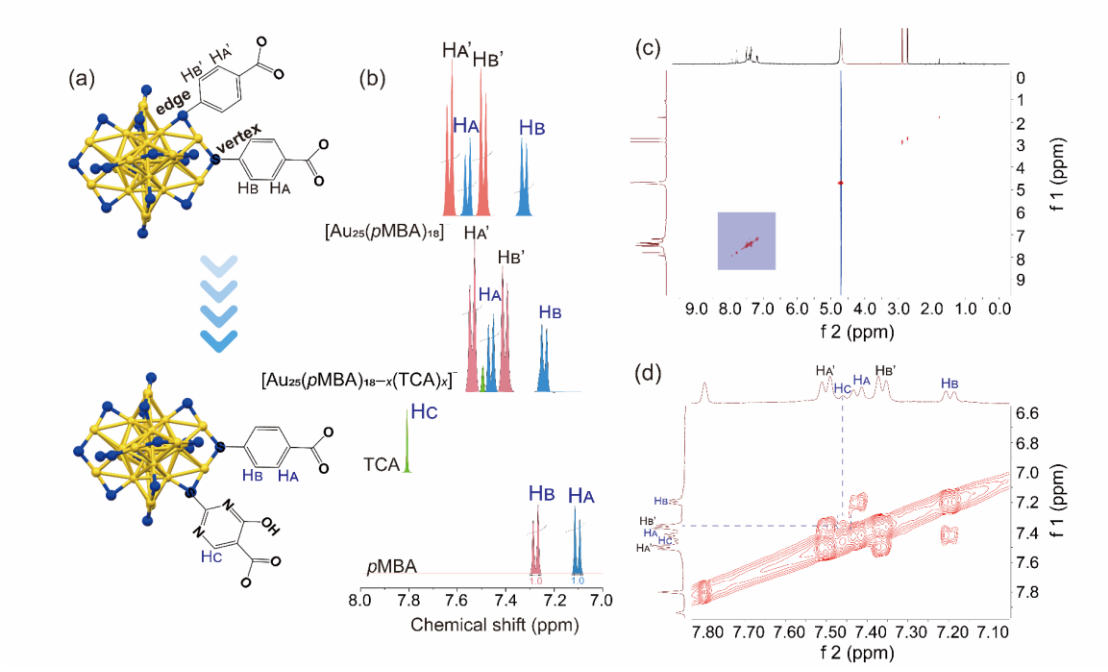

Figure 2. Molecular-level insights into ligand distribution on the surface of Au_{25} NCs. (a) Partial structural scheme of $[Au_{25}(pMBA)_{18}]^-$ and $[Au_{25}(pMBA)_{18-x}(TCA)_x]^-$. (b) ^1H NMR spectra of *p*MBA, TCA, $[Au_{25}(pMBA)_{18}]^-$, and $[Au_{25}(pMBA)_{18-x}(TCA)_x]^-$. (d) 2D ^1H-^1H NOESY spectra of $[Au_{25}(pMBA)_{18-x}(TCA)_x]^-$. (d) Zoom-in view of the boxed regions in (c). Color code: yellow Au, purple S.

To elucidate the role of ligand engineering in tuning the catalytic microenvironment, the electrocatalytic CO_2 reduction (CO_2RR) was conducted as a model reaction. The CO_2RR performance of $[Au_{25}(pMBA)_{18}]^-$ and $[Au_{25}(pMBA)_{18-x}(TCA)_x]^-$ was evaluated in a standard H-type cell using $KHCO_3$ as the electrolyte (0.1 M). Linear sweep voltammetry (LSV) was performed under the Ar and CO_2 atmosphere. As shown in Figure 3a, the LSV profiles of $[Au_{25}(pMBA)_{18}]^-$ and $[Au_{25}(pMBA)_{18-x}(TCA)_x]^-$ show higher current densities in the CO_2-saturated electrolyte than in the Ar-saturated electrolyte, suggesting the occurrence of CO_2RR in both cases. Moreover, $[Au_{25}(pMBA)_{18-x}(TCA)_x]^-$ shows a lower onset potential and higher current density for CO_2RR in the tested potential window compared with $[Au_{25}(pMBA)_{18}]^-$, providing clear evidence of the superior activity of the former toward CO_2RR. The controlled CO_2RR in a potentiostatic mode was conducted in a broad potential window from −0.5

to −1.6 V to investigate potential-dependent FE for CO generation (FE_{CO}). The only detected gaseous products were CO and H_2. Negligible liquid products, such as formic acid and methanol, were detected throughout the entire potentiostatic measurements (Figure S5 and S6). As shown in Figure 3b, $[Au_{25}(pMBA)_{18-x}(TCA)_x]^-$ exhibits higher CO selectivity across a broad potential range. Specifically, it exhibits a higher FE_{CO} over 90% within a relatively broad potential window from −0.6 to −1.4 V, whereas a FE of 98.6% was achieved at −0.9 V (CO current density of 15.5 mA/cm^2). Furthermore, $[Au_{25}(pMBA)_{18-x}(TCA)_x]^-$ requires a lower overpotential of 660 mV to reach a normalized CO partial current density (j_{CO}) of 10 mA/cm^2, whereas a similar overpotential required for $[Au_{25}(pMBA)_{18}]^-$ is approaching 900 mV (Figure S7). In terms of CO partial current density, $[Au_{25}(pMBA)_{18-x}(TCA)_x]^-$ yielded −15.5 mA/cm^2 at −0.9 V, which is significantly higher than −7.9 mA/cm^2 delivered by $[Au_{25}(pMBA)_{18}]^-$ at the same overpotential (Figure 3c). Further increasing the TCA substituted numbers led to a rise in j_{CO} with a flat FE_{CO} trend above 95% (Figure S8). Additionally, we compared the potential-dependent turnover frequency (TOF) of the two Au_{25} NCs. $[Au_{25}(pMBA)_{18-x}(TCA)_x]^-$ has a TOF of 38.8 s^{-1} at an applied potential of −0.9 V, which is approximately twice as that of $[Au_{25}(pMBA)_{18}]^-$ **(**Figure S9**)**. We also compared the highest TOF of $[Au_{25}(pMBA)_{18-x}(TCA)_x]^-$ with those of recently reported cluster-based electrocatalysts (Figure S10), suggesting that $[Au_{25}(pMBA)_{18-x}(TCA)_x]^-$ have a decent TOF conducive to practical application in electrocatalytic CO_2RR.

To gain insights into the electrocatalytic mechanism, Tafel analysis was performed to probe the rate-determining step (RDS) of CO_2RR. The RDS can be inferred from the dependency of current density on overpotentials.[42] Figure 3d depicts similar Tafel slopes of 144 and 141 mV dec^{-1} for $[Au_{25}(pMBA)_{18}]^-$ and $[Au_{25}(pMBA)_{18-x}(TCA)_x]^-$, respectively, suggesting that these two Au_{25} NCs share an identical RDS. To account for any possible difference in the electrochemical active surface area (ECSA) of these two Au_{25} NCs, the ECSA was normalized to the total current density and compared (Figure S11 and S12 and Figure 3e). The normalized ECSA of $[Au_{25}(pMBA)_{18-x}(TCA)_x]^-$ was consistently recorded as higher than that of $[Au_{25}(pMBA)_{18}]^-$**,** indicating that the activity of $[Au_{25}(pMBA)_{18-x}(TCA)_x]^-$ is slightly higher than that of $[Au_{25}(pMBA)_{18}]^-$. In addition, to rule out the decomposition of

organic ligands as a possible source of CO, we carried out a $^{13}CO_2$ isotopic labelling experiment. By supplying $^{13}CO_2$ in the CO_2RR, the enhanced production of ^{13}CO was clearly observed (Figure S13). It is worth noting that the minor signal of ^{13}CO observed before the supply of $^{13}CO_2$ could be attributed to the natural occurrence of the ^{13}C isotope in the atmosphere. The above results suggest that the improved electrocatalytic activity and selectivity of $[Au_{25}(pMBA)_{18-x}(TCA)_x]^-$ should be attributed to the regulation of the catalytic microenvironment enabled by the incorporation of TCA.

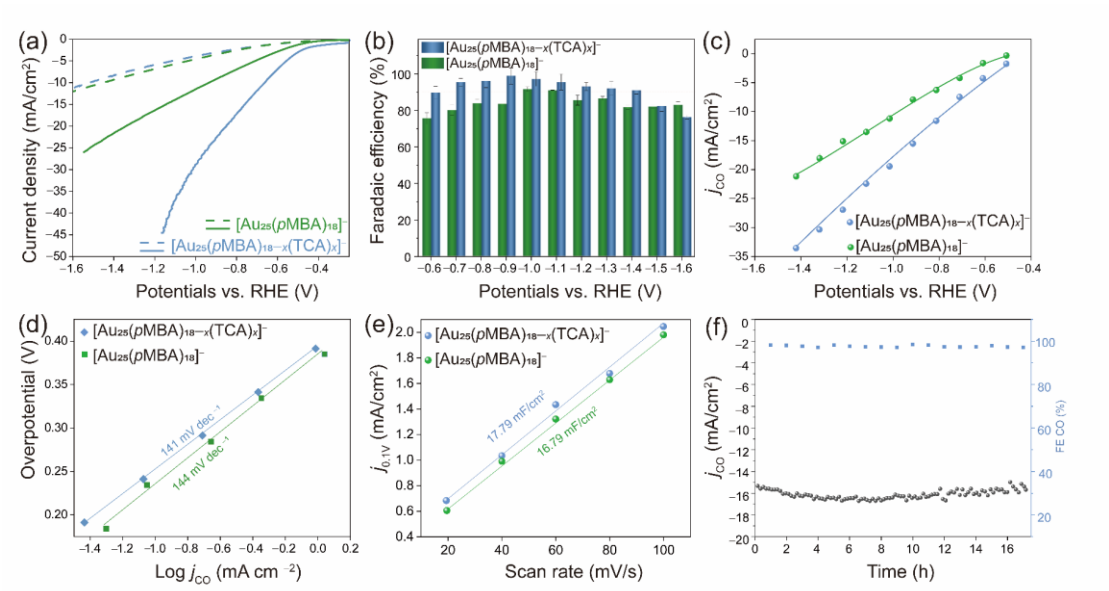

Figure 3. Electrocatalytic CO_2RR performance of $[Au_{25}(pMBA)_{18}]^-$ and $[Au_{25}(pMBA)_{18-x}(TCA)_x]^-$ in 0.1 M $KHCO_3$. (a) Linear sweep voltammetry (LSV) in quiescent Ar-purged and CO_2-saturated 0.1 M $KHCO_3$ solution (dashed and solid lines for the operating conditions in Ar and CO_2, respectively). (b) Faradaic efficiency (FE) of CO during CO_2RR. (c) Au molar number normalized CO partial current density (j_{CO}) at different cathodic potentials. (d) Tafel slopes. (e) Electrochemical surface-active area (ECSA). (f) Electrochemical stability test of $[Au_{25}(pMBA)_{18-x}(TCA)_x]^-$ at –0.9 V.

One notable concern associated with CO_2RR for metal NCs is the stability of the ligands during catalysis. Several studies have observed the dissociation of thiolate ligands during CO_2RR.[43-46] We have studied the stability of $[Au_{25}(pMBA)_{18-x}(TCA)_x]^-$ at –0.9 V over a time course of 16 h (Figure 3f). The FE_{CO} and j_{CO} maintain almost unchanged, suggesting good electrochemical stability of $[Au_{25}(pMBA)_{18-x}(TCA)_x]^-$ for

CO_2RR. The electrocatalysts were also examined by XPS analysis before and after long-term electrocatalysis. As shown in Figure S14, only a marginal increase (from 1.07 to 1.18) was recorded for the ratio of Au(I)/Au(0), indicating negligible decomposition of Au NCs during electrocatalysis. Of note, a common decomposition pathway of Au NCs is degradation into Au(I)-SR complexes. Moreover, the signal of N 1s peak for pyrimidine nitrogen remains almost unchanged in $[Au_{25}(p\text{MBA})_{18-x}(\text{TCA})_x]^-$after constant potential electrolysis (CPE) tests at both −0.6 and −0.9 V, implying that TCA was retained during CO_2RR in the low negative potential region (Figure S15). However, when the applied potential was increased to −1.6 V, the N 1s peak intensity faded, suggesting the removal of TCA at this high overpotential. This should be the root cause of the deteriorated performance of $[Au_{25}(p\text{MBA})_{18-x}(\text{TCA})_x]^-$ at high overpotentials.

Based on the identical RDS and similar ECSA of these two Au_{25} NC catalysts, we hypothesized that the enhanced catalytical activity and selectivity of $[Au_{25}(p\text{MBA})_{18-x}(\text{TCA})_x]^-$ could be attributed to the enhanced local CO_2 concentration. To verify this assertion, we compared the current density of generated CO (j_{CO}) and the corresponding FE_{CO} under different CO_2 partial pressures (P_{CO_2}) at 273 K. As shown in Figure 4a, a fitted log(j_{CO}) vs. log(P_{CO_2}) plot reflects the affinity between Au_{25} NCs and CO_2 molecules at a fixed potential of −0.9 V. The slope of this plot for $[Au_{25}(p\text{MBA})_{18-x}(\text{TCA})_x]^-$ is 0.087, indicating an approximate zero-order dependence on CO_2 concentration. As for $[Au_{25}(p\text{MBA})_{18}]^-$, the log($j_{CO}$) vs. log($P_{CO_2}$) plot shows a slope of 0.321, suggesting its propensity toward a first-order dependence on CO_2 concentration. In addition, the FE_{CO} for $[Au_{25}(p\text{MBA})_{18}]^-$ and $[Au_{25}(p\text{MBA})_{18-x}(\text{TCA})_x]^-$ were assessed in Figure 4b, where similar FE_{CO} values were recorded with CO_2 partial pressure up to 0.2 atm. Further increasing the CO_2 partial pressure to 1 atm led to a slightly higher FE_{CO} of $[Au_{25}(p\text{MBA})_{18-x}(\text{TCA})_x]^-$, in comparison to that of $[Au_{25}(p\text{MBA})_{18}]^-$. The close FE_{CO} between $[Au_{25}(p\text{MBA})_{18-x}(\text{TCA})_x]^-$ and $[Au_{25}(p\text{MBA})_{18}]^-$ indicates that the turnover capability of individual active sites should not be the dominant cause for the distinct difference in the catalytic activity of these two Au_{25} NCs, corroborating the role of local CO_2 enhancement in accelerating the CO_2RR kinetics. Besides, similar enzyme-like zero-order reaction kinetics were observed for $[Au_{25}(p\text{MBA})_{18-x}(\text{TCA})_x]^-$ at various

negative potentials (Figure 4c), where the FE_{CO} values of individual active sites remain consistent through the tested potential window (Figure 4d), indicating that the local CO_2 concentration on the active site surface was not significantly influenced by the CO_2 partial pressure due to the strong affinity of CO_2 and the TCA ligand.

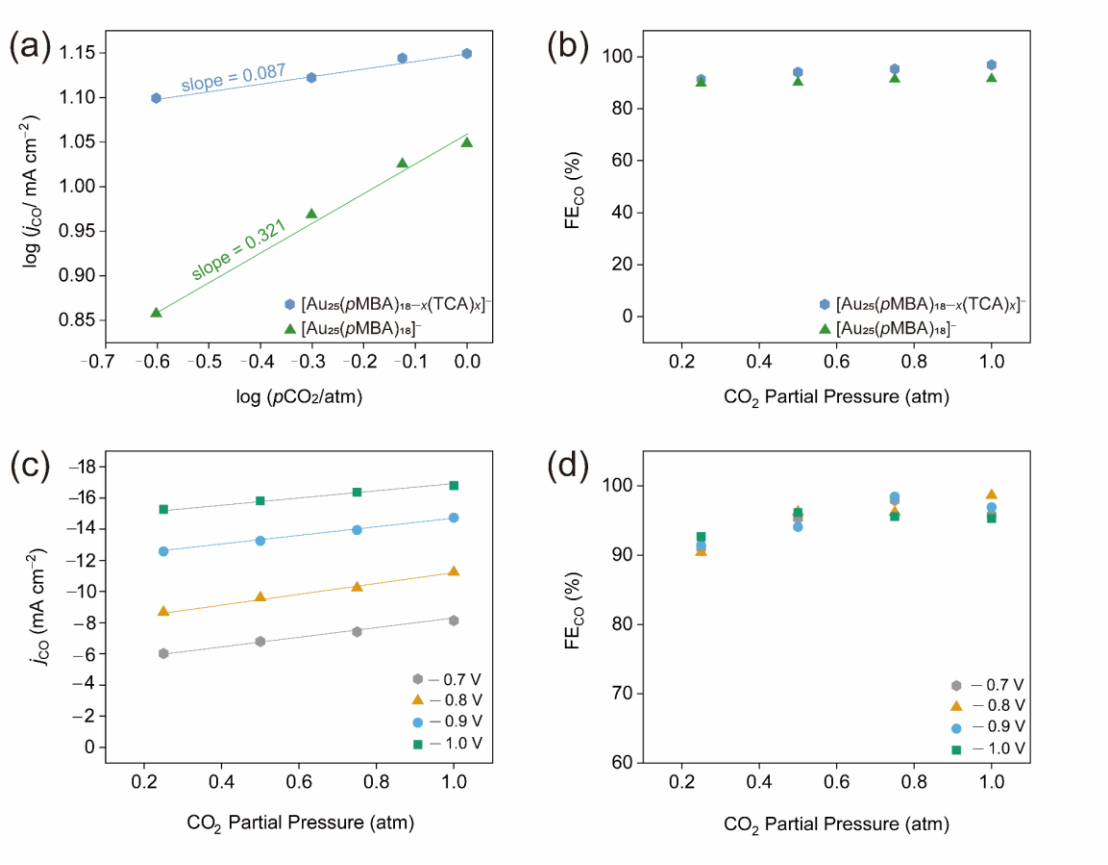

Figure 4. CO_2 partial pressure dependent kinetic study. (a) j_{CO} and (b) FE_{CO} on $[Au_{25}(pMBA)_{18}]^-$ and $[Au_{25}(pMBA)_{18-x}(TCA)_x]^-$ at −0.9 V in 0.1 M $KHCO_3$. (c) j_{CO} and (d) FE_{CO} on $[Au_{25}(pMBA)_{18-x}(TCA)_x]^-$ at various potentials.

The enhanced affinity of CO_2 to $[Au_{25}(pMBA)_{18-x}(TCA)_x]^-$ was further supported by CO_2 adsorption experiments on free TCA and *p*MBA molecules. The uptake curves of TCA and *p*MBA recorded at 298 K manifest up to 7 times higher uptake by TCA over *p*MBA (Figure S16). This enhanced uptake by TCA should be attributed to the affinity of electropositive pyrimidine N of TCA to electronegative C of CO_2. The strong affinity enables $[Au_{25}(pMBA)_{18-x}(TCA)_x]^-$ to have a faster CO_2 accumulation near the active sites compared with $[Au_{25}(pMBA)_{18}]^-$ (Figure 5a), which could boost the kinetics of CO_2RR. This data was further supported by the CO_2 binding energies on

both ligands from density functional theory (DFT) calculations. We found that TCA possesses stronger binding with CO_2 than *p*MBA (Figure S17). In other words, TCA can better extract CO_2 molecules and bring them closer to the active sites on the cluster surface than *p*MBA. Such enhanced affinity of TCA to CO_2 can thus be readily transmitted to $[Au_{25}(pMBA)_{18-x}(TCA)_x]^-$, as evidenced by our UV-vis absorption and ESI-MS analyses. A previous study has shown that CO_2 adsorption can alter the electronic structure and cause subtle changes in the UV-vis absorption spectrum.[47] After bubbling CO_2 into the purified aqueous solution of $[Au_{25}(pMBA)_{18-x}(TCA)_x]^-$, a slight bleaching of the absorption feature at ~700 nm was observed (Figure 5b), which agrees well with the previous observation of a slight electron withdrawal by CO_2.[47] More direct evidence of preferential CO_2 adsorption on $[Au_{25}(pMBA)_{18-x}(TCA)_x]^-$ comes from ESI-MS analysis on their aqueous solution saturated by CO_2, where an important adduct of $[Au_{25}(pMBA)_{16}(TCA)_2+2CO_2-3H]^{4-}$ was successfully captured (Figure 5c). The formula of captured adduct also suggests that every TCA molecule is able to adsorb one CO_2 molecule, supportive to the TCA-assisted CO_2 adsorption mechanism. By sharp contrast, similar CO_2 adducts were not observed in the ESI-MS spectrum of $[Au_{25}(pMBA)_{18}]^-$ in a similar CO_2-saturated solution (Figure S18), suggesting the relatively weaker affinity of CO_2 to $[Au_{25}(pMBA)_{18}]^-$. It should be noted that capturing catalytic intermediates in CO_2RR is a nontrivial undertaking, and our ESI-MS results may represent a marked advance in uncovering the electrocatalytic mechanism of CO_2RR on Au NCs or nanoparticles at the atomic level.[48-50] Such strong affinity of $[Au_{25}(pMBA)_{18-x}(TCA)_x]^-$ for CO_2 molecules poses a significant implication for dilute or mixed gases containing CO_2 in electrocatalytic conversion without the need for a concentrating or separating step. Of note, the strong affinity affinity of $[Au_{25}(pMBA)_{18-x}(TCA)_x]^-$ for CO_2 also allows us to estimate the adsorption behavior at varied partial pressure of CO_2, which can be well fitted by the Langmuir model (Figure S19).

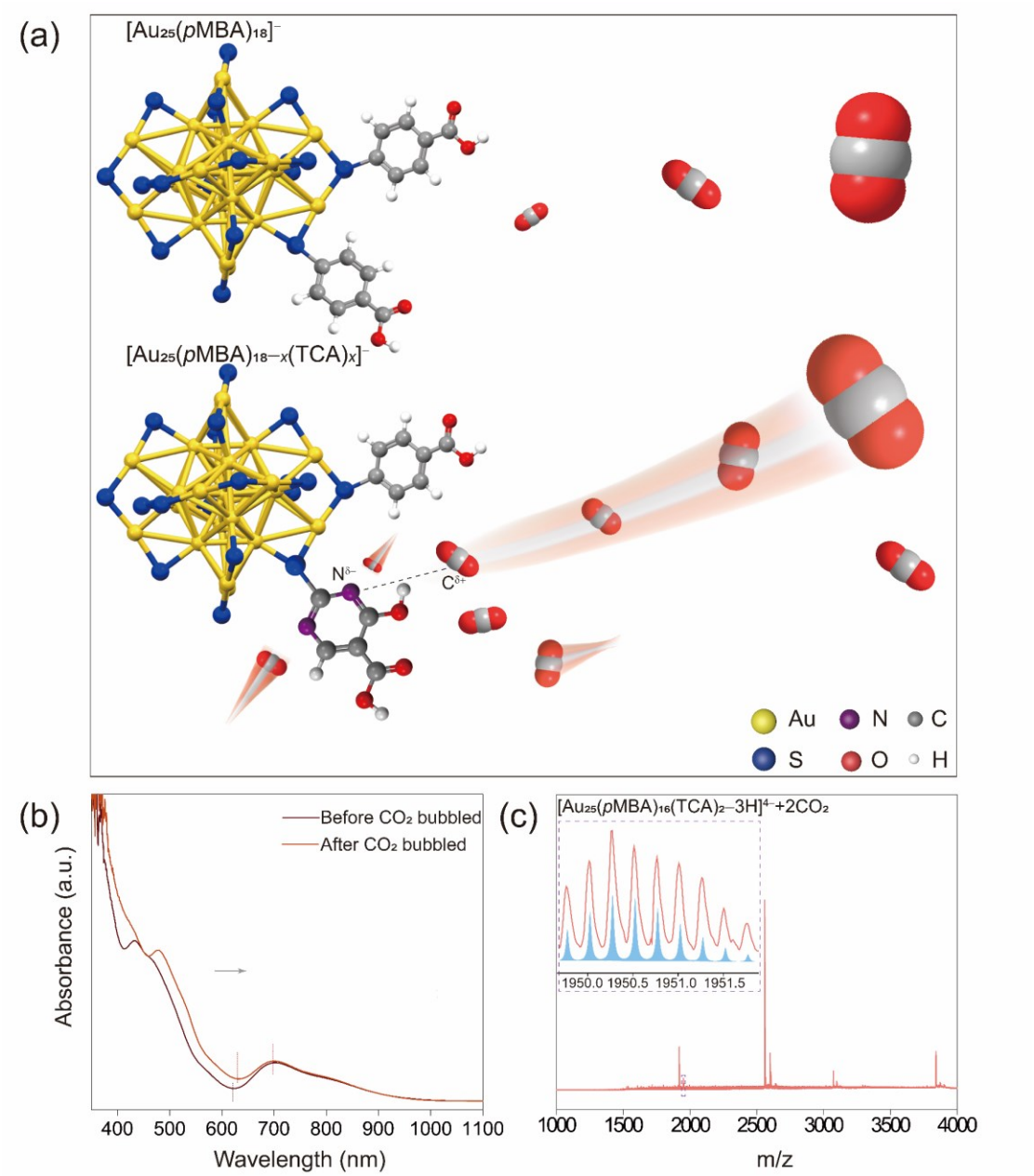

Figure 5. Molecular interactions between $[Au_{25}(pMBA)_{18-x}(TCA)_x]^-$ and CO_2. (a) Schematic illustration of the affinity between Au_{25} NCs and CO_2 molecules. (b) UV-vis absorption spectra of $[Au_{25}(pMBA)_{18-x}(TCA)_x]^-$ before and after bubbling CO_2. (c) ESI-MS spectra of $[Au_{25}(pMBA)_{18-x}(TCA)_x]^-$ after bubbling CO_2 (the insert is the isotope patterns of cluster ions, confirming the accuracy of mass spectrum assignment, where the filled line depicts the calculated isotope pattens of $[Au_{25}(pMBA)_{16}(TCA)_2-3H]^{4-}+2CO_2$).

In the context of preferential CO_2 adsorption on $[Au_{25}(pMBA)_{18-x}(TCA)_x]^-$, we further studied the effects of TCA on the mass transfer profiles of CO_2. CO_2 concentration gradient distribution simulation was utilized to estimate the mass transfer efficiency based on a steady-state model established in the reported CO_2RR studies (See more details in section Modelling, SI). Figure S20 describes the electrode-electrolyte boundary layer in the CO_2RR system. The analysis suggests that the resistances to mass transfer are likely to occur in the hydrodynamic boundary layer, with a thickness to be approximately 40 to 50 μm based on the limiting current density of 22 mA cm^{-2}. The small current density is attributed to the lower solubility of CO_2 (0.0342 M) and the lower buffer concentration (0.1 M) in the electrolyte.[51] The concentration gradient in this interfacial region (within 50 μm from the surface of electrode) was calculated at steady state, taking into account the interplay between CO_2RR and HER activities. Notably, we simulated the CO_2 diffusion gradient from the bulk electrolyte to the outer layer of the NCs instead of the active surface itself to eliminate any interference from the chemo-adsorption of CO_2 on the active sites. As shown in Figure S21, the application of a cathodic potential disrupts the uniform CO_2 concentration between the electrode surface (i.e., outer layer of the NCs) and bulk electrolyte in both cases. This disruption creates a diffusion layer as a result of CO_2 consumption and transport. However, it can be clearly seen that a concentration difference of CO_2 can be induced at the outer layer of these two types of Au_{25} NCs due to the varied protecting ligands at the same cathodic potential. This difference is attributed to the strong affinity of the TCA ligand toward CO_2, which accelerates the transport of CO_2 from the outer layer to the surface of the active sites, creating a higher local concentration of CO_2 near the active sites. The mass transfer modelling indicates a greater concentration gradient for $[Au_{25}(pMBA)_{18-x}(TCA)_x]^-$, suggesting a faster consumption of CO_2 on the surface of TCA-modified Au_{25} NCs. This implies that a faster mass transfer rate of CO_2 from TCA to active sites can be achieved due to the greater concentration gradient, resulting in higher CO_2 conversion on $[Au_{25}(pMBA)_{18-x}(TCA)_x]^-$.

Conclusions

In conclusion, we have precisely incorporated a secondary pyrimidine-containing thiolate ligand into the protecting layer of atomically precise Au_{25} NCs, and

investigated the ligand's effect on tuning the microenvironment of Au_{25} cluster catalysts for CO_2RR. The molecular-level distribution of these two ligands on Au NCs, including their number and position, was elucidated. The precise surface ligand engineering demonstrated in this study results in Au NCs with an enhanced local CO_2 concentration near the active sites. This enhancement led to high reactivity and selectivity for CO production (FE of 98.6% and TOF of 39 s^{-1} at –0.9 V). Notably, the CO_2 reduction selectivity for CO remains independent of CO_2 partial pressure, suggesting that this ligand modification has significant potential in CO_2RR under dilute CO_2 concentration conditions, which are common in industrial application scenarios. Mechanistic investigations reveal that the strong affinity of the pyrimidine ligand for CO_2 leads to the *in-situ* accumulation of CO_2 surrounding the active Au sites, thereby boosting the kinetics of CO_2RR. The affinity between CO_2 molecules and TCA was qualitatively and quantitively evidenced through optical absorption and mass spectrum analyses. These findings exemplify a rational design on molecular modification aimed at tuning the surface microenvironment of electrocatalysts, providing insights for the development of efficient molecular catalysts for CO_2RR.

Associated Content

Supporting Information

The Supporting Information is available free of charge at ****.

Experimental of gold nanocluster synthesis and purification; electrode preparation; electrochemical measurement; electrospray ionization mass spectrometry; UV-vis absorption spectrum; fitted Langmuir model plots; additional computational methods including density functional theory calculations and modelling simulations; XPS test; ^1H NMR spectrometry; overpotentials and TOF analysis and comparison; CV test; GC-MS test; CO_2 adsorption isotherms test; electrode-electrolyte boundary layer and CO_2 concentration gradients analysis.

Author Information

Corresponding Authors

Jianping Xie - Department of Chemical and Biomolecular Engineering, National University of Singapore, 117585, Singapore; Joint School of National University of Singapore and Tianjin University International Campus of Tianjin University Binhai New City, Fuzhou 350207, P. R. China; Email: **chexiej@nus.edu.sg**

Qiaofeng Yao – Key Laboratory of Organic Integrated Circuits, Ministry of Education & Tianjin Key Laboratory of Molecular Optoelectronic Sciences, Department of Chemistry, School of Science, Tianjin University, Tianjin 300072, China; Collaborative Innovation Center of Chemical Science and Engineering (Tianjin), Tianjin 300072, China; Email: **qfyao@tju.edu.cn**

De-en Jiang - Department of Chemical and Biomolecular Engineering, Vanderbilt University, Nashville, TN, 37212, USA; Email: **de-en.jiang@vanderbilt.edu**

Lei Wang - Department of Chemical and Biomolecular Engineering, National University of Singapore, 117585, Singapore; Email: **wanglei8@nus.edu.sg**

Authors

Zhihe Liu - Department of Chemical and Biomolecular Engineering, National University of Singapore, 117585, Singapore; Joint School of National University of Singapore and Tianjin University International Campus of Tianjin University Binhai New City, Fuzhou 350207, P. R. China

Junmei Chen - Department of Chemical and Biomolecular Engineering, National University of Singapore, 117585, Singapore

Bo Li - Department of Chemical and Biomolecular Engineering, Vanderbilt University, Nashville, TN, 37212, USA

Notes

The authors declare no competing financial interest.

Acknowledgements

We acknowledge the National University of Singapore, Ministry of Education, Singapore for their financial support, through the Academic Research Fund (AcRF) Grant No. R-279-000-580-112 and A-8000054-01-00, Centre for Hydrogen

Innovations at NUS(CHI-P2023-01). J. Xie and Q. Yao would also like to acknowledge the support by the National Natural Science Foundation of China (22071174, 22371204). L. Wang would like to thank the support from A*STAR (Agency for Science, Technology and Research) under its LCERFI program (Award No U2102d2002), and the support by National Research Foundation (NRF) Singapore, under NRF Fellowship (NRF-NRFF13-2021-0007). D.J. (DFT computation) was supported by the National Science Foundation (Award number: CHE-2245564).

References

(1) Chakraborty, I.; Pradeep, T. Atomically Precise Clusters of Noble Metals: Emerging Link between Atoms and Nanoparticles. *Chem. Rev.* **2017**, *117*, 8208-8271

(2) Guan, Z.-J.; Li, J.-J.; Hu, F.; Wang, Q.-M. Structural Engineering toward Gold Nanocluster Catalysis. *Angew. Chem. Int. Ed.* **2022**, *61*, e202209725

(3) Kim, D.; Yu, S.; Zheng, F.; Roh, I.; Li, Y.; Louisia, S.; Qi, Z.; Somorjai, G. A.; Frei, H.; Wang, L.-W.; et al. Selective CO_2 electrocatalysis at the pseudocapacitive nanoparticle/ordered-ligand interlayer. *Nat. Energy* **2020**, *5*, 1032-1042

(4) Wang, Z.; Gupta, R. K.; Alkan, F.; Han, B.-L.; Feng, L.; Huang, X.-Q.; Gao, Z.-Y.; Tung, C.-H.; Sun, D. Dicarboxylic Acids Induced Tandem Transformation of Silver Nanocluster. *J. Am. Chem. Soc.* **2023**, *145*, 19523-19532

(5) Yun, Y.; Sheng, H.; Bao, K.; Xu, L.; Zhang, Y.; Astruc, D.; Zhu, M. Design and Remarkable Efficiency of the Robust Sandwich Cluster Composite Nanocatalysts ZIF-8@Au_{25}@ZIF-67. *J. Am. Chem. Soc.* **2020**, *142*, 4126-4130

(6) Fang, Y.; Bao, K.; Zhang, P.; Sheng, H.; Yun, Y.; Hu, S.-X.; Astruc, D.; Zhu, M. Insight into the Mechanism of the CuAAC Reaction by Capturing the Crucial Au_4Cu_4–π-Alkyne Intermediate. *J. Am. Chem. Soc.* **2021**, *143*, 1768-1772

(7) Du, Y.; Sheng, H.; Astruc, D.; Zhu, M. Atomically Precise Noble Metal Nanoclusters as Efficient Catalysts: A Bridge between Structure and Properties. *Chem. Rev.* **2020**, *120*, 526-622

(8) Tan, Y.; Sun, G.; Jiang, T.; Liu, D.; Li, Q.; Yang, S.; Chai, J.; Gao, S.; Yu, H.; Zhu, M. Symmetry Breaking Enhancing the Activity of Electrocatalytic CO_2 Reduction on an Icosahedron-Kernel Cluster by Cu Atoms Regulation. *Angew. Chem. Int. Ed.* **2024**, *63*, e202317471

(9) Wang, Y.; Zhang, W.; Wen, W.; Yu, X.; Du, Y.; Ni, K.; Zhu, Y.; Zhu, M. Atomically Dispersed Unsaturated Cu-N_3 Sites on High-Curvature Hierarchically Porous Carbon Nanotube for Synergetic Enhanced Nitrate Electroreduction to Ammonia. *Adv. Funct. Mater.* **2023**, *33*, 2302651

(10) Yao, Q.; Yuan, X.; Chen, T.; Leong, D. T.; Xie, J. Engineering Functional Metal Materials at the Atomic Level. *Adv. Mater.* **2018**, *30*, 1802751

(11) Liu, Z.; Tan, H.; Li, B.; Hu, Z.; Jiang, D.-e.; Yao, Q.; Wang, L.; Xie, J. Ligand Effect on Switching the Rate-determining Step of Water Oxidation in Atomically Precise Metal Nanoclusters. *Nat.Commum.* **2023**, *14*, 3374

(12) Heaven, M. W.; Dass, A.; White, P. S.; Holt, K. M.; Murray, R. W. Crystal Structure of the Gold Nanoparticle $[N(C_8H_{17})_4][Au_{25}(SCH_2CH_2Ph)_{18}]$. *J. Am. Chem. Soc* **2008**, *130*, 3754-3755

(13) Yao, Q.; Liu, L.; Malola, S.; Ge, M.; Xu, H.; Wu, Z.; Chen, T.; Cao, Y.; Matus, M. F.; Pihlajamäki, A.; et al. Supercrystal Engineering of Atomically Precise Gold Nanoparticles Promoted by Surface Dynamics. *Nat.Chem.* **2023**, *15*, 230-239

(14) Narouz, M. R.; Osten, K. M.; Unsworth, P. J.; Man, R. W. Y.; Salorinne, K.; Takano, S.; Tomihara, R.; Kaappa, S.; Malola, S.; Dinh, C.-T.; et al. N-heterocyclic Carbene-functionalized Magic-number Gold Nanoclusters. *Nat.Chem.* **2019**, *11*, 419-425

(15) Gao, Z.-H.; Wei, K.; Wu, T.; Dong, J.; Jiang, D.-e.; Sun, S.; Wang, L.-S. A Heteroleptic Gold Hydride Nanocluster for Efficient and Selective Electrocatalytic Reduction of CO_2 to CO. *J. Am. Chem. Soc.* **2022**, *144*, 5258-5262

(16) Kulkarni, V. K.; Khiarak, B. N.; Takano, S.; Malola, S.; Albright, E. L.; Levchenko, T. I.; Aloisio, M. D.; Dinh, C.-T.; Tsukuda, T.; Häkkinen, H.; et al. N-Heterocyclic Carbene-Stabilized Hydrido Au_{24} Nanoclusters: Synthesis, Structure, and Electrocatalytic Reduction of CO_2. *J. Am. Chem. Soc.* **2022**, *144*, 9000-9006

(17) Yuan, S.-F.; He, R.-L.; Han, X.-S.; Wang, J.-Q.; Guan, Z.-J.; Wang, Q.-M. Robust Gold Nanocluster Protected with Amidinates for Electrocatalytic CO_2 Reduction. *Angew. Chem. Int. Ed.* **2021**, *60*, 14345-14349

(18) Wang, J.; Xu, F.; Wang, Z. Y.; Zang, S. Q.; Mak, T. C. W. Ligand-Shell Engineering of a Au_{28} Nanocluster Boosts Electrocatalytic CO_2 Reduction. *Angew. Chem. Int. Ed.* **2022**, *61*, e202207492

(19) Li, S.; Nagarajan, A. V.; Li, Y.; Kauffman, D. R.; Mpourmpakis, G.; Jin, R. The Role of Ligands in Atomically Precise Nanocluster-catalyzed CO_2 Electrochemical Reduction. *Nanoscale* **2021**, *13*, 2333-2337

(20) Epstein, I. R.; Xu, B. Reaction–diffusion Processes at the Nano- and Microscales. *Nat. Nanotechnol.* **2016**, *11*, 312-319

(21) Liu, X.; Appelhans, D.; Voit, B. Hollow Capsules with Multiresponsive Valves for Controlled Enzymatic Reactions. *J. Am. Chem. Soc.* **2018**, *140*, 16106-16114

(22) Ragsdale, S. W. Metals and Their Scaffolds To Promote Difficult Enzymatic Reactions. *Chem. Rev.* **2006**, *106*, 3317-3337

(23) Kim, C.; Bui, J. C.; Luo, X.; Cooper, J. K.; Kusoglu, A.; Weber, A. Z.; Bell, A. T. Tailored Catalyst Microenvironments for CO_2 Electroreduction to Multicarbon Products on Copper using Bilayer Ionomer Coatings. *Nat. Energy* **2021**, *6*, 1026-1034

(24) Zhou, X.; Liu, H.; Xia, B. Y.; Ostrikov, K.; Zheng, Y.; Qiao, S.-Z. Customizing the Microenvironment of CO_2 Electrocatalysis via Three-phase Interface Engineering. *SmartMat* **2022**, *3*, 111-129

(25) Goyal, A.; Marcandalli, G.; Mints, V. A.; Koper, M. T. M. Competition between CO_2 Reduction and Hydrogen Evolution on a Gold Electrode under Well-Defined Mass Transport Conditions. *J. Am. Chem. Soc* **2020**, *142*, 4154-4161

(26) Zhang, B.; Jiang, Y.; Gao, M.; Ma, T.; Sun, W.; Pan, H. Recent Progress on Hybrid Electrocatalysts for Efficient Electrochemical CO_2 Reduction. *Nano Energy* **2021**, *80*, 105504

(27) Chen, J.; Liu, X.; Xi, S.; Zhang, T.; Liu, Z.; Chen, J.; Shen, L.; Kawi, S.; Wang, L. Functionalized Ag with Thiol Ligand to Promote Effective CO_2 Electroreduction. *ACS Nano* **2022**, *16*, 13982-13991

(28) Zhao, Y.; Liu, X.; Chen, J.; Chen, J.; Chen, J.; Fan, L.; Yang, H.; Xi, S.; Shen, L.; Wang, L. Promote Electroreduction of CO_2 via Catalyst Valence State Manipulation by Surface-capping Ligand. *Proc. Natl. Acad. Sci. U. S. A.* **2023**, *120*, e2218040120

(29) Kuhl, K. P.; Hatsukade, T.; Cave, E. R.; Abram, D. N.; Kibsgaard, J.; Jaramillo, T. F. Electrocatalytic Conversion of Carbon Dioxide to Methane and Methanol on Transition Metal Surfaces. *J. Am. Chem. Soc* **2014**, *136*, 14107-14113

(30) Chen, J.; Wang, L. Effects of the Catalyst Dynamic Changes and Influence of the Reaction Environment on the Performance of Electrochemical CO_2 Reduction. *Adv. Mater.* **2022**, *34*, 2103900

(31) Strmcnik, D.; Kodama, K.; van der Vliet, D.; Greeley, J.; Stamenkovic, V. R.; Marković, N. M. The Role of Non-covalent Interactions in Electrocatalytic Fuel-cell Reactions on Platinum. *Nat. Chem.* **2009**, *1*, 466-472

(32) Monteiro, M. C. O.; Dattila, F.; Hagedoorn, B.; García-Muelas, R.; López, N.; Koper, M. T. M. Absence of CO_2 Electroreduction on Copper, Gold and Silver Electrodes without Metal Cations in Solution. *Nat. Cata.* **2021**, *4*, 654-662

(33) Zhang, X.; Li, J.; Li, Y.-Y.; Jung, Y.; Kuang, Y.; Zhu, G.; Liang, Y.; Dai, H. Selective and High Current CO_2 Electro-Reduction to Multicarbon Products in Near-Neutral KCl Electrolytes. *J. Am. Chem. Soc* **2021**, *143*, 3245-3255

(34) Liu, M.; Pang, Y.; Zhang, B.; De Luna, P.; Voznyy, O.; Xu, J.; Zheng, X.; Dinh, C. T.; Fan, F.; Cao, C.; et al. Enhanced Electrocatalytic CO_2 Reduction via Field-induced Reagent Concentration. *Nature* **2016**, *537*, 382-386

(35) Chen, Q.; Luo, M.; Hammershøj, P.; Zhou, D.; Han, Y.; Laursen, B. W.; Yan, C.-G.; Han, B.-H. Microporous Polycarbazole with High Specific Surface Area for Gas Storage and Separation. *J. Am. Chem. Soc* **2012**, *134*, 6084-6087

(36) Liao, P.-Q.; Zhou, D.-D.; Zhu, A.-X.; Jiang, L.; Lin, R.-B.; Zhang, J.-P.; Chen, X.-M. Strong and Dynamic CO_2 Sorption in a Flexible Porous Framework Possessing Guest Chelating Claws. *J. Am. Chem. Soc* **2012**, *134*, 17380-17383

(37) An, J.; Geib, S. J.; Rosi, N. L. High and Selective CO_2 Uptake in a Cobalt Adeninate Metal−Organic Framework Exhibiting Pyrimidine- and Amino-Decorated Pores. *J. Am. Chem. Soc* **2010**, *132*, 38-39

(38) Zito, A. M.; Clarke, L. E.; Barlow, J. M.; Bím, D.; Zhang, Z.; Ripley, K. M.; Li, C. J.; Kummeth, A.; Leonard, M. E.; Alexandrova, A. N.; et al. Electrochemical Carbon Dioxide Capture and Concentration. *Chem. Rev.* **2023**, *123*, 8069-8098

(39) Yao, Q.; Yuan, X.; Fung, V.; Yu, Y.; Leong, D. T.; Jiang, D.-e.; Xie, J. Understanding Seed-mediated Growth of Gold Nanoclusters at Molecular level. *Nat. Commun.* **2017**, *8*, 927

(40) Zhu, M.; Yao, Q.; Liu, Z.; Zhang, B.; Lin, Y.; Liu, J.; Long, M.; Xie, J. Surface Engineering Assisted Size and Structure Modulation of Gold Nanoclusters by Ionic Liquid Cations. *Angew. Chem. Int. Ed.* **2022**, *61*, e202115647

(41) Suzuki, W.; Takahata, R.; Chiga, Y.; Kikkawa, S.; Yamazoe, S.; Mizuhata, Y.; Tokitoh, N.; Teranishi, T. Control over Ligand-Exchange Positions of Thiolate-Protected Gold Nanoclusters Using Steric Repulsion of Protecting Ligands. *J. Am. Chem. Soc.* **2022**, *144*, 12310-12320

(42) Liu, S.; Tao, H.; Zeng, L.; Liu, Q.; Xu, Z.; Liu, Q.; Luo, J.-L. Shape-Dependent Electrocatalytic Reduction of CO_2 to CO on Triangular Silver Nanoplates. *J. Am. Chem. Soc.* **2017**, *139*, 2160-2163

(43) Sun, Y.; Liu, X.; Xiao, K.; Zhu, Y.; Chen, M. Active-Site Tailoring of Gold Cluster Catalysts for Electrochemical CO_2 Reduction. *ACS Catal.* **2021**, *11*, 11551-11560

(44) Seong, H.; Efremov, V.; Park, G.; Kim, H.; Yoo, J. S.; Lee, D. Atomically Precise Gold Nanoclusters as Model Catalysts for Identifying Active Sites for Electroreduction of CO_2. *Angew. Chem. Int. Ed.* **2021**, *60*, 14563-14570

(45) Sun, F.; Qin, L.; Tang, Z.; Deng, G.; Bootharaju, M. S.; Wei, Z.; Tang, Q.; Hyeon, T. –SR Removal or –R Removal? A Mechanistic Revisit on the Puzzle of Ligand Etching of $Au_{25}(SR)_{18}$ Nanoclusters during Electrocatalysis. *Chem. Sci.* **2023**, *14*, 10532-10546

(46) Seong, H.; Jo, Y.; Efremov, V.; Kim, Y.; Park, S.; Han, S. M.; Chang, K.; Park, J.; Choi, W.; Kim, W.; et al. Transplanting Gold Active Sites into Non-Precious-Metal Nanoclusters for Efficient CO_2-to-CO Electroreduction. *J. Am. Chem. Soc.* **2023**, *145*, 2152-2160

(47) Kauffman, D. R.; Alfonso, D.; Matranga, C.; Qian, H.; Jin, R. Experimental and Computational Investigation of Au_{25} Clusters and CO_2: A Unique Interaction and Enhanced Electrocatalytic Activity. *J. Am. Chem. Soc.* **2012**, *134*, 10237-10243

(48) Nam, D.-H.; De Luna, P.; Rosas-Hernández, A.; Thevenon, A.; Li, F.; Agapie, T.; Peters, J. C.; Shekhah, O.; Eddaoudi, M.; Sargent, E. H. Molecular enhancement of heterogeneous CO_2 reduction. *Nat. Mater.* **2020**, *19*, 266-276

(49) Clark, E. L.; Resasco, J.; Landers, A.; Lin, J.; Chung, L.-T.; Walton, A.; Hahn, C.; Jaramillo, T. F.; Bell, A. T. Standards and Protocols for Data Acquisition and Reporting for Studies of the Electrochemical Reduction of Carbon Dioxide. *ACS Cata.* **2018**, *8*, 6560-6570

(50) Sullivan, I.; Goryachev, A.; Digdaya, I. A.; Li, X.; Atwater, H. A.; Vermaas, D. A.; Xiang, C. Coupling Electrochemical CO_2 Conversion with CO_2 Capture. *Nat. Cata.* **2021**, *4*, 952-958

(51) Singh, M. R.; Goodpaster, J. D.; Weber, A. Z.; Head-Gordon, M.; Bell, A. T. Mechanistic Insights into Electrochemical Reduction of CO_2 over Ag using Density Functional Theory and Transport Models. *Proc. Natl. Acad. Sci. U. S. A.* **2017**, *114*, E8812-E8821